Materials Today Bio 16 (2022) 100446

Contents lists available at ScienceDirect

Materials Today Bio

journal homepage: www.journals.elsevier.com/materials-today-bio

Attachment of −*t*Bu groups to aza-BODIPY core at 3,5-sites with ultra-large Stokes shift to enhance photothermal therapy through apoptosis mechanism

Ran Li [a,1], Junyi Ren [b,1], Dongxiang Zhang [a,1], Meiheng Lv [a], Zhan Wang [b], Huan Wang [b], Shan Zhang [b], Jianjun Du [c,**], Xin-Dong Jiang [a,*], Guiling Wang [b,***]

[a] Liaoning & Shenyang Key Laboratory of Functional Dye and Pigment, Shenyang University of Chemical Technology, Shenyang, 110142, China
[b] Department of Cell Biology, China Medical University, Shenyang, 110122, China
[c] State Key Laboratory of Fine Chemicals, Dalian University of Technology, Dalian, 116024, China

ARTICLE INFO

Keywords:
Aza-BODIPY
Tert-butyl group
Stokes shift
Photothermal therapy
Near-infrared

ABSTRACT

By the introduction of the −*t*Bu groups into aza-BODIPY core, di-*tert*-butyl-substituted aza-BODIPYs at 3,5-sites (**tBuazaBDPs**) were prepared for the first time. Based on the X-ray analysis of **CN-tBuazaBDP**, this molecular structure is twisted. Near-infrared dye **SMe-tBuazaBDP** has the ultra-large Stokes shift (152 nm) in aza-BODIPY system, combining with the twisted intramolecular charge transfer and the free rotation of the −*t*Bu groups at 3,5-sites. Although the barrier-free rotors of the distal −*t*Bu groups in **SMe-tBuazaBDP** result in low fluorescence quantum yield, the photothermal conversion efficiency is markedly enhanced. **SMe-tBuazaBDP** nanoparticles with low power laser irradiation were proven to block cancer cell cycle, inhibit cancer cell proliferation, and induce cancer cell apoptosis in photothermal therapy (PTT). The strategy of "direct attachment of −*t*Bu groups to aza-BODIPY core" gives a new design platform for a photothermal therapy agent.

1. Introduction

Cancers seriously threaten human life and health. So, drug therapy has become a widespreadly used treatment for cancers since 1942 [1–5]. However, the intractable problems of high toxicity, side effects and drug resistance are still the main obstacles in clinical drug treatment of cancer. Recently, phototherapeutic, as a burgeoning tumor therapy method, has been developed rapidly with advantages of high spatial-temporal resolution, non-invasive property and low side effects [6–8]. Phototherapeutic mainly involves two species of treatments, photodynamic therapy (PDT) and photothermal therapy (PTT) [9–12]. PDT depends upon the efficient intersystem crossing (ISC) of the triplet photosensitizers (PSs) to sensitize the oxygen to produce reactive oxygen species (ROS) [13–15]. PTT converts light energy into heat by photothermal agents to increase the temperature of the surrounding environment, resulting in localized thermal damage [16–18]. Compared with PDT, the advantage of PTT is not restricted by the tumor hypoxic environment [19]. However, the high temperature (≥47 °C) could lead to a damage to the normal tissues and may be also prone to inflammation and tumor metastasis [20,21]. Therefore, based on American National Standard for Safe Use of Lasers Outdoors, the maximum permissible exposure (MPE) for skin exposure is 0.2 W cm^{-2} at the 635 nm laser [22,23]. So, the temperature for the safe PTT under low laser power density should be slightly above 42 °C (usually 42–46 °C) [20,21]. A relaxed molecule in the lowest vibrational level of the excited state is known to return to the ground state mainly via the radiative transition (fluorescent emission), the non-radiative transition (heat release) and ISC to the triplet, sensitizing oxygen to produce ROS, that is, three channels to release energy [24,25]. Therefore, according to the Jablonski energy level diagram [26], by restricting the release of fluorescence and strengthening the other energy release process, the combination of PTT/PDT could maximize the effect of tumor treatment.

Aza-borondipyrromethene (aza-BODIPY) as a classic dye is known to widespreadly applied in fluorescence imaging, phototherapy, photocatalysis and optoelectronic materials and so forth, owing to its near-infrared (NIR) absorption characteristic, high molar extinction

* Corresponding author.
** Corresponding author.
*** Corresponding author.
E-mail addresses: dujj@dlut.edu.cn (J. Du), xdjiang@syuct.edu.cn (X.-D. Jiang), glingwang@cmu.edu.cn (G. Wang).
[1] These authors contributed equally.

https://doi.org/10.1016/j.mtbio.2022.100446
Received 10 August 2022; Received in revised form 26 September 2022; Accepted 28 September 2022
Available online xxxx

coefficient and excellent stability [27–30]. Since differential structure of aza-BODIPY determines its specific optical property [31], it is of great significance to tune the molecular structure of aza-BODIPY to meet the requirements of high performance application for PTT/PDT. Especially, aza-BODIPY-based photothermal dyes have been attracting increasing interest as the important photothermal reagents, because of high photothermal conversion efficiency [32–36]. For example, Zhao and Dong et al. introduced a pH-sensitive receptor into the aza-BODIPY core, and the photodynamic and photothermal therapies are achieved by pH-triggered mechanism. Meantime, the therapeutic effect can be tracked by photoaccoustic and photothermal dual-imaging [33–36]. We also noticed that aza-BODIPY-based photothermal reagents were only extended and expanded on the basis of tetraphenyl aza-BODIPY (**PhazaBDP**) derivatives in aza-BODIPY system (Fig. 1a) [37]. Very recently, three cases of non-aryl substituted aza-BODIPYs at 1,7-sites were reported, including an example of our group (Fig. 1b) [38–40]. We focused on design and application of aza-BODIPYs, which paves the avenue for us to break through the traditional aza-BODIPY structure [41–44]. Herein, we synthesized the non-aryl substituted aza-BODIPYs at 3,5-sites (**tBuazaBDP**s) for the first time (Fig. 1c), breaking the structural restrictions of the traditional dye **PhazaBDP** and opening up a significative highway for the structural innovation in aza-BODIPY system. The free rotation effect of the –*t*Bu group in aza-BODIPY could enhance the non-radiative transition process (Fig. 1a) [39], which provided an ideal design platform for photothermal reagent [45]. So, in this work for some specific uses it would be beneficial to replace –Ph with –*t*Bu group at 3, 5-sites, though this would need to be achieved without loss of their valuable photophysical properties. It is worth mentioning that, **tBuazaBDP**s have excellent spectral properties with large Stokes shift and high molar extinction coefficient at the cost of loss of long wavelength absorption, which could be compensated by the push-pull system. **SMe-tBuazaBDP** has the ultra-large Stokes shift (152 nm) in aza-BODIPY family, combining with the twisted intramolecular charge transfer (TICT) [46] and the free rotation of the –*t*Bu groups at 3,5-sites. Especially, **SMe-tBuazaBDP** has low fluorescence quantum yield, and this contrarily achieved the programme of the excited state to enhance the non-radiative transition for exploring PTT/PDT. Furthermore, **SMe-tBuazaBDP** nanoparticles (**SMe-tBuazaBDP** NPs) were prepared to improve the water solubility and biocompatibility. Since the photothermal radiation with different intensity could usually trigger cell death through either necrosis or apoptosis [47,48], however PTT through apoptosis mechanism is rarely reported, comparing to necrosis mechanism [17]. In this work, **SMe-tBuazaBDP** under low laser radiation of 0.2 W cm^{-2}, was proven to inhibit cell viability, block cell cycle, inhibit cancer cell proliferation, induce cancer cell apoptosis, and lead to the death of cancer cells.

2. Experimental section

2.1. General

All chemical reagents and organic solvents were analytical grade, purchased from Energy Chemical & Technology (Shanghai) Co. Ltd without further purification unless otherwise specified. ^{1}H NMR spectra were recorded on a VARIAN Mercury 500 MHz spectrometer. ^{1}H NMR chemical shifts (δ) are given in ppm downfield from Me_4Si, determined by residual chloroform ($\delta = 7.26$ ppm). ^{13}C NMR spectra were recorded on a VARIAN Mercury 125 MHz spectrometer in $CDCl_3$, reporting in ppm with the internal chloroform signal at $\delta = 77.0$ ppm as standard. A high resolution mass spectrometer is used to give the exact molecular weight of the product. Fluorescence spectra were recorded on an F-128 spectrophotometer and are reported as cm^{-1}. Absorption spectrogram were recorded on a UV-2550 spectrophotometer at 298 K. The absolute fluorescence quantum yield was measured by F-98 spectrophotometer. Laser particle size analyzer purchased from Malvern. The temperature of the solution is monitored by a temperature measuring camera. A 635 nm laser was applied as the light source for light irradiation, controlling by a fiber coupled laser system for the laser output power and purchased from Changchun New Industries Optoelectronics Technology. Optical power density was measured by a CEL-NP 2000 power meter, purchased from Beijing Zhong Jiao Jin Yuan Technology Co, Ltd. BioTek Synergy H1 microplate reader was used in CCK8 assay. Confocal laser fluorescence microscope FV1200 (Olympus, Japan) was applied to estimate fluorescence imaging.

2.2. X-ray analysis

Crystals suitable for the X-ray structural determination were mounted on a Mac Science DIP2030 imaging plate diffractometer and irradiated with graphite monochromated Mo-Kα radiation (λ = 0.71073 Å) for the data collection. The unit cell parameters were determined by separately

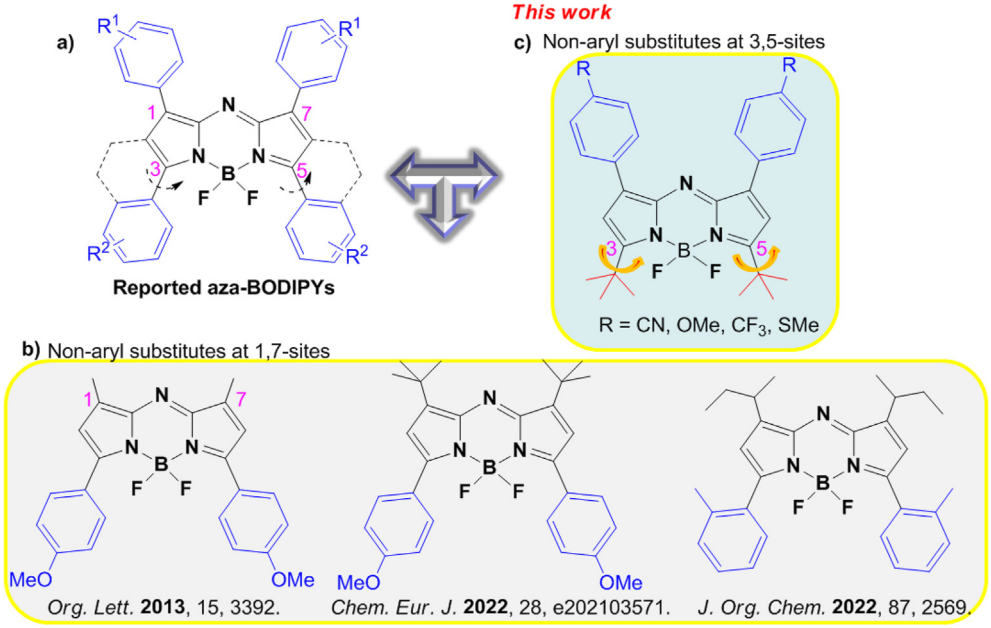

Fig. 1. Design strategies for **tBuazaBDP**s with the –*t*Bu groups at 3,5-sites.

auto-indexing several images in each data set using the DENZO program (MAC Science). For each data set, the rotation images were collected in 3° increments with a total rotation of 180° about the φ axis. The data were processed using SCALEPACK. The structures were solved by a direct method with the SHELX-97 program. Refinement on F^2 was carried out using the full-matrix least-squares by the SHELX-97 program. All non-hydrogen atoms were refined using the anisotropic thermal parameters. The hydrogen atoms were included in the refinement along with the isotropic thermal parameters.

2.3. Theoretical details

All theoretical calculations were performed based on density functional theory (DFT) and time-dependent density functional theory (TDDFT) methods via Gaussian 16 program suite. Becke's three-parameter hybrid exchange function with Lee-Yang-Parr gradient-corrected correlation functional (B3LYP) and 6-31G(D) basis set were selected to serve the calculations. And the solvation effects of dichloromethane were also taken into consideration with the solvation model based on density (SMD).

2.4. Preparation of SMe-tBuazaBDP nanoparticles (SMe-tBuazaBDP NPs)

1 ml THF solution containing 1 mg **SMe-tBuazaBDP** and 5 mg DSPE-PEG_{2000} is slowly and gradually added to the 10 ml aqueous solution. Subsequently, THF was volatilized by vigorous stirring for 24 h with the purpose of dye molecules dispersed into the solution equably. The desired **SMe-tBuazaBDP** NPs could be obtained by centrifugation at 6000 rpm for 5 min.

2.5. Evaluation of singlet oxygen ($^1O_2$) production efficiency

As the capture agent of $^1O_2$, 1,3-diphenlisobenzofuran (DPBF) can indicate the production capacity of $^1O_2$ in the solution. When the photosensitized agent produces $^1O_2$ under light radiation, DPBF will react with $^1O_2$ to open the loop, decreasing the absorption value at 416 nm. The absorption decline slope of DPBF can preliminarily guide the capacity of $^1O_2$ production. Meanwhile, the $^1O_2$ production efficiency of the dyes can be calculated by the following formula under the reference 2,6-diiodobodipy with known $^1O_2$ production rate efficiency ($\Phi_\Delta = 0.85$ in toluene).

$$\varphi_{\mathrm{sam}} = \varphi_{\mathrm{BDP}}\left(\frac{m_{sam}}{m_{BDP}}\right)\left(\frac{F_{BDP}}{F_{sam}}\right)$$

where "*sam*" represents the unknown dye molecule and "*BDP*" represents the reference 2,6-diiodobodipy. "*m*" is the slope of DPBF absorption peak decline, "*F*" is the absorption correction factor, $F = 1\text{-}10^{-\mathrm{O.D.}}$. O.D. represents the absorption value of the sample at the wavelength of light radiation.

2.6. Measurement of photothermal capacity

The temperature change of dye nanoparticles in aqueous solution was evaluated by using 635 nm laser with different power density and different concentration of nanoparticles solution. The cooling process is under natural cooling. The temperature of the solution was measured by a temperature camera. The photothermal conversion efficiency is calculated using the reported formula [16–18]. For instance, **SMe-tBuazaBDP** NPs aqueous solution (80 μM) was irradiated by a 635 nm laser (0.3 W cm^{-2}) for 10 min. Then, the solution was cooled to room temperature naturally, and the temperature was monitored every 1 min.

The calculation of photothermal conversion efficiency was based on the previously reported studies, and the specific calculation method was described by the following formula.

$$\eta = \left(hs(T_{max} - T_{surr}) - Q_{Dis}\right) / \left(I \times \left(1 - 10^{-A}\right)\right)$$

Among them, η represents photothermal conversion efficiency, h is the heat transfer coefficient, s is the surface area of the container, Q_{Dis} represents heat dissipated from the laser mediated by the solvent and container. I is the laser power and A is the absorbance at 635 nm.

$$hs = mC_{H2O}/\tau_s$$

m is the mass of the solution containing the PTAs, C is the specific heat capacity of the solution, and τ_s is the associated time constant.

$$T = -\tau_s\, ln(\theta)$$

θ is a dimensionless parameter, known as the driving force temperature.

$$\theta = (T - T_{surr}) / (T_{max} - T_{surr})$$

T is the current temperature. T_{Max} and T_{Surr} represent the maximum steady state temperature and the environmental temperature, respectively.

2.7. Evaluation of cytotoxicity by CCK8 assay

Human colon cancer (SW-620) cells or gastric cancer (SGC-7901) cells were cultured in 96-well plates for 24 h. The cells were treated with different treatments including no treatment (control group), **SMe-tBuazaBDP** NPs treatment, light treatment and **SMe-tBuazaBDP** NPs with light treatment, and different illumination time gradients (0–40 min) were added to light group and NPs with light group to evaluate the suitable time of light radiation to **SMe-tBuazaBDP** NPs. The cells were added with **SMe-tBuazaBDP** NPs (30 μM) and then cultured for 2 h, followed by irradiation at 635 nm (0.2 W cm^{-2}, 20 min), and then cultured for 2 h. After that, Cell Counting Kit-8 (CCK8) was added to each well for further cultivation for 2 h. The absorbance value at 450 nm was measured by a microplate reader.

2.8. AM/PI staining of live-dead cells

Human colon cancer (SW-620) cells or gastric cancer (SGC-7901) cells were cultured in a 24-well plate for imaging experiments. The cells were treated in different groups to evaluate the dark-toxicity and phototoxicity of **SMe-tBuazaBDP** NPs. *Group 1*: natural growth (control group); *Group 2*: 30 μM dye NPs treatment (dye group); *Group 3*: 635 nm radiation (0.2 W cm^{-2} for 20 min) as light group; *Group 4*: After the dye NPs entered the cell (30 μM), 635 nm radiation (0.2 W cm^{-2} for 20 min) was applied as dye NPs + light group. After continuing culture for 30 min, Calcein-AM/PI double stain kit was added into each group of cells, continuing culture for 30 min for confocal fluorescence imaging. Among them, Calcein AM emits green fluorescence to indicate living cells with excitation wavelength of 488 nm and fluorescence collection channel of 500–529 nm, while PI emits red fluorescence to indicate dead cells with excitation wavelength of 559 nm and fluorescence collection channel of 570–619 nm.

2.9. Cell cycle analysis by flow cytometry

Human gastric cancer (SGC-7901) cells were cultured in 6-well plates for 24 h. The cells were treated in different groups to evaluate the dark-toxicity and photo-toxicity of **SMe-tBuazaBDP** NPs. *Group 1*: natural growth (control group); *Group 2*: 30 μM dye NPs treatment (dye group); *Group 3*: 635 nm radiation (0.2 W cm^{-2} for 20 min) as light group; *Group 4*: After the dye NPs entered the cell (30 μM), 635 nm radiation (0.2 W cm^{-2} for 20 min) was applied as dye NPs + light group. After continuing culture for 2 h, adherent cells were harvested by trypsinization and washed with cold PBS. Subsequently, the cells were fixed with ice-cold 70% ethanol at 4 °C overnight. Before analysis, ethanol was discarded

and propidium iodide was used to stain the cells for 1 h in the dark. Then, the treated cells were subjected to flow cytometric analysis using the BD FACSVerse™ Flow Cytometer. A total of 10,000 events were acquired for each sample.

2.10. Cell apoptosis analysis by annexin-v/propidium iodide

Human gastric cancer (SGC-7901) cells were cultured in 6-well plates and treated in different groups. *Group 1*: natural growth (control group); *Group 2*: 30 μM dye NPs treatment (dye group); *Group 3*: 635 nm radiation (0.2 W cm^{-2} for 20 min) as light group; *Group 4*: After the dye NPs entered the cell (30 μM), 635 nm radiation (0.2 W cm^{-2} for 20 min) was applied as dye NPs + light group. Cells after treatment were collected by trypsinization, and then the extent of apoptosis was evaluated by using the Annexin V/FITC apoptosis detection kit (Beyotime Biotechnology). Cells were analyzed immediately by using the BD LSRFortessa (BD Biosciences) flow cytometer.

2.11. mRNA levels related to cell growth by RT-qPCR

Human gastric cancer (SGC-7901) cells were cultured in 6-well plates and treated in different groups. *Group 1*: natural growth (control group); *Group 2*: 30 μM dye NPs treatment (dye group); *Group 3*: 635 nm radiation (0.2 W cm^{-2} for 20 min) as light group; *Group 4*: After the dye NPs entered the cell (30 μM), 635 nm radiation (0.2 W cm^{-2} for 20 min) was applied as dye NPs + light group. Total RNA was isolated by the TRIzol method (Tiangen) and reverse transcribed into cDNA using the RevertAid Reverse Transcription Premix (Thermo Fisher Scientific). Quantitative PCR was performed on an ABI-7900 system using ChamQ Universal SYBR qPCR Master Mix (Vazyme Biotech).

2.12. Protein levels related to cell growth by western blot

Human gastric cancer (SGC-7901) cells were cultured in 6-well plates and treated in different groups. *Group 1*: natural growth (control group); *Group 2*: 30 μM dye NPs treatment (dye group); *Group 3*: 635 nm radiation (0.2 W cm^{-2} for 20 min) as light group; *Group 4*: After the dye NPs entered the cell (30 μM), 635 nm radiation (0.2 W cm^{-2} for 20 min) was applied as dye NPs + light group. For western blot, control and treated cells for different groups were harvested and washed thoroughly with 1 × cold PBS. Cell lysates were prepared by extracting the proteins by using radio-immuno precipitation assay (RIPA) buffer. The lysates were clarified by centrifugation at 13,000 rpm for 20 min at 4 °C, and collected in fresh centrifuge tube. The protein concentrations of the extracted lysates were measured using Coomassie Brilliant Blue (CBB). Equal amounts of denatured protein were separated by SDS-PAGE and transferred to a PVDF membrane. The membrane was blocked with non-fat dry milk for 1 h at room temperature, and the proteins were probed with following antibodies: Bcl-2 (Affinit, 1:1000), cyclin D1 (ABclonal, 1:1000), c-myc (ABclonal, 1:1000) and β-tubulin (proteintech, 1:1000). After overnight incubation, the membranes were washed with TBS-t, and then incubated with respective secondary peroxidase-conjugated antibodies for 1 h at room temperature and developed using chemiluminescence reagent. Finally, the detection was performed with a chemiluminescence detection system (MF-ChemiBIS 3.2).

2.13. Synthesis (Scheme 1)

2.13.1. Synthesis of 3(E)-4-(4,4-dimethyl-3-oxopent-1-enyl)benzonitrile (1-CN)

3,3-Dimethylbutan-2-one (0.48 ml, 3.8 mmol) was added to 4-formylbenzonitrile (500 mg, 3.8 mmol) in 20 ml methanol. Then 2 g KOH in 1 ml H_2O was added to the mixture, and this mixture was refluxed for 6 h. After cooling to room temperature, the solvents were removed by evaporation, and the resulting crude mixture was separated by column chromatography (CH_2Cl_2/*n*-hexane = 1:2) to afford dark brown liquid as compound **1-CN** (570 mg, 2.7 mmol, 71%). ^{1}H NMR (400 MHz, $CDCl_3$): δ (ppm) 7.83 (d, ^3J = 8.0 Hz, 2H), 7.67 (d, ^3J = 16 Hz, 1H), 7.65 (d, ^3J = 8.0 Hz, 2H), 7.18 (d, ^3J = 16 Hz, 1H), 1.24 (s, 9H). ^{13}C NMR (125 MHz, $CDCl_3$): δ (ppm) 204.1, 168.5, 141.4, 138.6, 134.4, 128.5, 128.1, 122.8, 43.5, 26.3.

2.13.2. Synthesis of 4-(5,5-dimethyl-1-nitro-4-oxohexan-2-yl)benzonitrile (2-CN)

Triethylamine (2 ml) and nitromethane (1.5 ml) were added to **1-CN** (0.57 g, 2.7 mmol) in anhydrous methanol (20 ml). The mixture was refluxed for 8 h. After cooling to room temperature, the solvent was removed under reduced pressure, and resulting crude mixture was separated by column chromatography (*n*-hexane: CH_2Cl_2 = 1:1) to afford **2-CN** (0.44 g, 1.6 mmol, 59%) as dark brown liquid. ^{1}H NMR (400 MHz, $CDCl_3$): δ (ppm) 7.80 (d, ^3J = 8.0 Hz, 1H), 7.60 (d, ^3J = 8.0 Hz, 1H), 7.42 (d, ^3J = 8.0 Hz, 1H), 7.32 (d, ^3J = 8.0 Hz, 1H), 4.67 (dd, ^2J = 16.0 Hz, ^3J = 8.0 Hz 2H), 4.07–4.11 (m, 1H), 2.93–2.99 (m, 2H), 1.07 (s, 9H). ^{13}C NMR (125 MHz, $CDCl_3$): δ (ppm) 212.3, 166.1, 143.4, 132.5, 128.0, 127.2, 50.2, 42.1, 39.1, 29.8, 26.3.

2.13.3. Synthesis of *CN-tBuazaBDP*

NH_4OAc (10 g, 129.7 mmol) was added to a suspension of compound **2-CN** (0.44 g, 1.6 mmol) in a mixture of anhydrous methanol (20 ml). The mixture was refluxed for 8 h. After cooling to room temperature, the mixture was extracted with CH_2Cl_2 (2 × 50 ml), and the organic layer was washed with brine (2 × 50 ml) and dried over anhydrous Na_2SO_4. After solvent removal by evaporation, the residue **3-CN** was dissolved in 10 ml anhydrous $ClCH_2CH_2Cl$. Triethylamine (0.5 ml, 3.6 mmol) was added and stirred at room temperature for 2 h, followed by dropwise addition of $BF_3{\cdot}Et_2O$ (1 ml, 7.9 mmol) with stirring at room temperature for 2 h. The mixture was then heated in 70 °C for 2 h. After cooling to room temperature, the mixture was extracted with CH_2Cl_2 (2 × 50 ml), and the organic layer was washed with brine (2 × 50 ml) and dried over anhydrous Na_2SO_4. After solvent removal by evaporation, and the resulting crude product was separated by column chromatography (CH_2Cl_2/*n*-hexane = 2:1) to afford **CN-tBuazaBDP** (142 mg, 0.28 mmol, 35%) as a dark red solid. ^{1}H NMR (500 MHz, $CDCl_3$): δ (ppm) 7.98 (d, ^3J = 8.5 Hz, 4H), 7.71 (d, ^3J = 8.5 Hz, 4H), 6.89 (s, 2H), 1.56 (s, 18H). ^{13}C NMR (125 MHz, $CDCl_3$): δ (ppm) 145.1, 136.9, 133.2, 132.6, 130.1, 128.9, 119.0, 113.0, 112.4, 36, 30.5. HRMS (ESI) *m/z* calcd for $C_{30}H_{28}BF_2N_5Na^+$ $(M + Na)^+$ 530.22980, found 530.23041.

2.13.4. Synthesis of *1-CF$_3$*

4-(Trifluoromethyl)benzaldehyde (0.44 ml, 2.9 mmol) was used as the starting material, and **1-CF$_3$** was obtained as reddish-brown solids (515.1 mg, 2.0 mmol, 69%). ^{1}H NMR (500 MHz, $CDCl_3$): δ (ppm) 7.59 (d, ^3J = 15.5 Hz, 1H), 7.58 (d, ^3J = 8.0 Hz, 2H), 7.52 (d, ^3J = 8.0 Hz, 2H), 7.15 (d, ^3J = 15.5 Hz, 1H), 1.15 (s, 9H).

2.13.5. Synthesis of *2-CF$_3$*

1-CF$_3$ (515.1 mg, 2.0 mmol) was used as the starting material, and **2-CF$_3$** was obtained as reddish-brown solids (350.9 mg, 1.1 mmol, 55%). ^{1}H NMR (500 MHz, $CDCl_3$): δ (ppm) 7.15 (d, ^3J = 8.0 Hz, 2H), 7.11 (d, ^3J = 8.0 Hz, 2H), 4.68 (dd, ^2J = 12.5 Hz, ^2J = 6.0 Hz, 1H), 4.59 (dd, ^2J = 12.5 Hz, ^2J = 6.0 Hz, 1H), 4.07 (quint, ^3J = 6.0 Hz, 1H), 2.97 (dd, ^2J = 12.5 Hz, ^2J = 6.0 Hz, 1H), 2.87 (dd, ^2J = 12.5 Hz, ^2J = 6.0 Hz, 1H), 0.98 (s, 9H).

2.13.6. Synthesis of *CF$_3$-tBuazaBDP*

2-CF$_3$ (350.9 mg, 1.1 mmol) was used as the starting material, and ***CF$_3$-tBuazaBDP*** was obtained as reddish-brown solids (137.8 mg, 0.23 mmol, 42%). ^{1}H NMR (500 MHz, $CDCl_3$): δ (ppm) 8.01 (d, ^3J = 8.0 Hz, 4H), 7.66 (d, ^3J = 8.0 Hz, 4H), 6.88 (s, 2H), 1.57 (s, 18H). ^{13}C NMR (125 MHz, $CDCl_3$): δ (ppm) 173.7, 144.6, 142.1, 135.6, 130.8, 129.3, 125.3, 123.0, 118.1, 35.3, 30.0. HRMS (ESI) *m/z* calcd for $C_{30}H_{28}BF_8N_3Na^+$ $(M + Na)^+$ 616.21408, found 616.21423.

*2.13.7. Synthesis of **1-OMe***

4-Methoxybenzaldehyde (0.45 g, 3.7 mmol) was used as the starting material, and **1-OMe** was obtained as reddish-brown solids (545.1 mg, 2.5 mol, 67%). ^{1}H NMR (500 MHz, $CDCl_3$): δ (ppm) 7.55 (d, ^3J = 15 Hz, 1H), 7.41 (d, ^3J = 8.5 Hz, 2H), 6.94 (d, ^3J = 15 Hz, 1H), 6.77 (d, ^3J = 8.5 Hz, 2H), 3.67 (s, 3H), 1.12 (s, 9H).

*2.13.8. Synthesis of **2-OMe***

1-OMe (545.1 mg, 2.5 mmol) was used as the starting material, and **2-OMe** was obtained as reddish-brown solids (390.6 mg, 1.4 mmol, 56%).

*2.13.9. Synthesis of **OMe-tBuazaBDP***

2-OMe (390.6 mg, 1.4 mmol) was used as the starting material, and ***OMe-tBuazaBDP*** was obtained as reddish-brown solids (79.6 mg, 0.15 mmol, 22%). ^{1}H NMR (500 MHz, $CDCl_3$): δ (ppm) 7.95 (d, ^3J = 9.0 Hz, 4H), 6.95 (d, ^3J = 9.0 Hz, 4H), 6.71 (s, 2H), 3.88 (s, 6H), 1.55 (s, 18H). ^{13}C NMR (125 MHz, $CDCl_3$): δ (ppm) 160.5, 146.9, 143.1, 130.7, 125.4, 124.3, 123.8, 118.9, 55.2, 34.9, 31.2. HRMS (ESI) *m/z* calcd for $C_{30}H_{34}BF_2N_3O_2Na^+$ $(M + Na)^+$ 540.26044, found 540.26074.

*2.13.10. Synthesis of **1-SMe***

4-(Methylthio)benzaldehyde (0.44 ml, 3.3 mmol) was used as the starting material, and **1-SMe** was obtained as reddish-brown solids (461.9 mg, 1.97 mmol, 60%). ^{1}H NMR (500 MHz, $CDCl_3$): δ (ppm) ^{1}H NMR (500 MHz, $CDCl_3$): δ (ppm) 7.63 (d, ^3J = 15.2 Hz, 1H), 7.48 (d, ^3J = 8.0 Hz, 2H), 7.33 (d, ^3J = 8.0 Hz, 2H), 7.07 (d, ^3J = 15.2 Hz, 1H), 2.51 (s, 3H), 1.22 (s, 9H).

*2.13.11. Synthesis of **2-SMe***

1-SMe (461.9 mg, 1.97 mmol) was used as the starting material, and

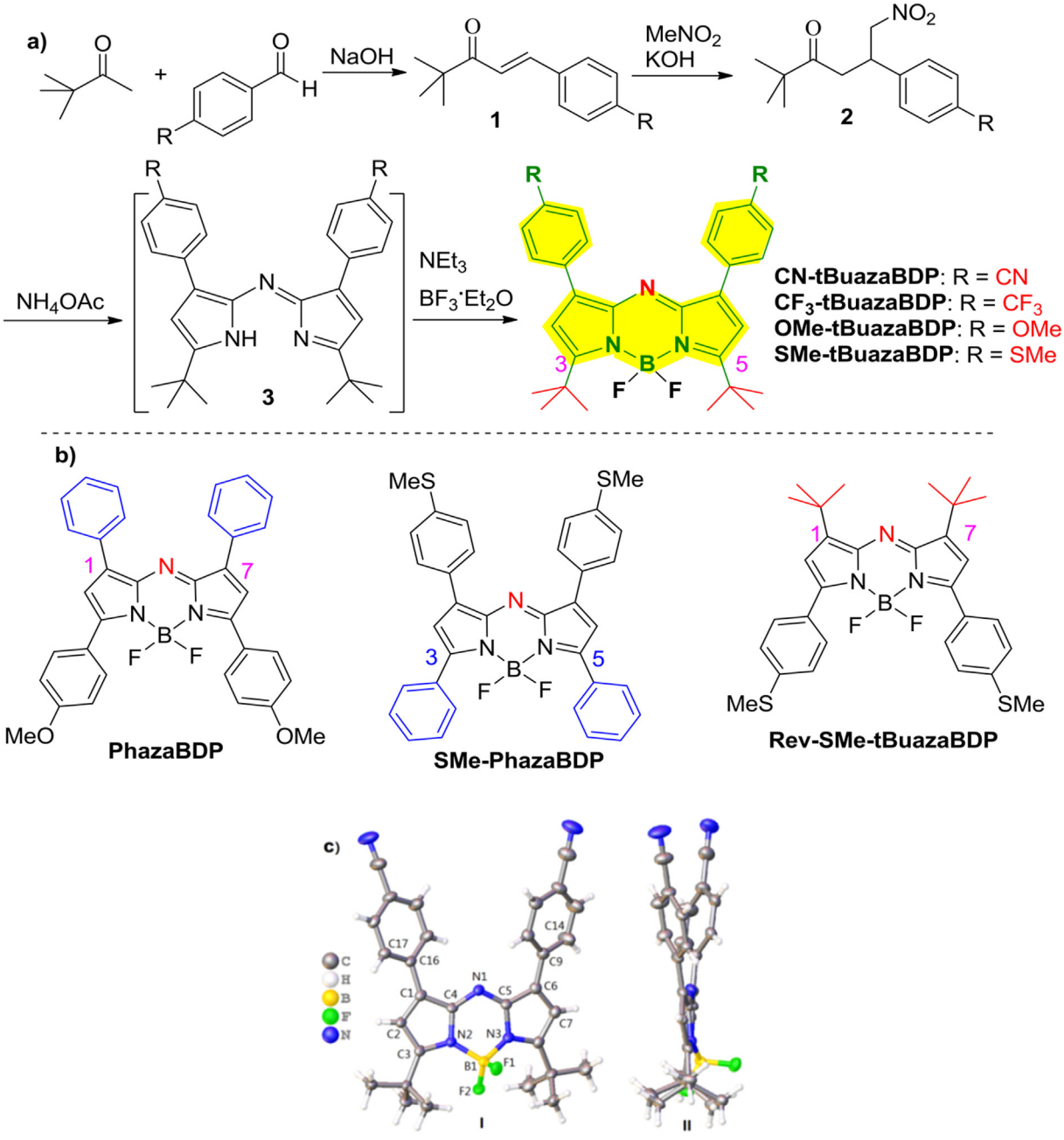

Scheme 1. a) Synthesis of dyes **R-tBuazaBDP**s (R = CF_3, CN, OMe, SMe) with 3,5-di-*tert*-butyl groups at 3,5-sites. b) Molecular structures of dyes. c) ORTEP views of ***CN*-tBuazaBDP** (CCDC: 2,150,981) (displacement ellipsoids at the 30% probability level). (I) Front, (II) side of molecular structure.

2-SMe was obtained as reddish-brown solids (291.1 mg, 0.98 mmol, 50%). ^{1}H NMR (500 MHz, $CDCl_3$): δ (ppm) 7.15 (d, ^3J = 8.5 Hz, 2H), 7.11 (d, ^3J = 8.5 Hz, 2H), 4.64 (dd, ^2J = 12.5 Hz, ^2J = 6.5 Hz, 1H), 4.55 (dd, ^2J = 12.5 Hz, ^2J = 6.5 Hz, 1H), 3.96 (quint, ^3J = 6.5 Hz, 1H), 2.94 (dd, ^2J = 12.5 Hz, ^2J = 6.5 Hz, 1H), 2.84 (dd, ^2J = 12.5 Hz, ^2J = 6.5 Hz, 1H), 2.51 (s, 3H), 1.05 (s, 9H).

2.13.12. Synthesis of SMe-tBuazaBDP

2-SMe (291.1 mg, 1 mmol) was used as the starting material, and ***SMe-tBuazaBDP*** was obtained as reddish-brown solids (135.4 mg, 0.246 mmol, 49%). ^{1}H NMR (500 MHz, $CDCl_3$): δ (ppm) 7.92 (d, ^3J = 8.5 Hz, 4H), 7.27 (d, ^3J = 8.5 Hz, 4H), 6.75 (s, 2H), 2.54 (s, 6H), 1.55 (s, 18H). ^{13}C NMR (125 MHz, $CDCl_3$): δ (ppm) 140.5, 129.4, 129.1, 127.3, 127.1, 126.6, 126.3, 125.7, 35.1, 29.9, 15.2. HRMS (ESI) *m/z* calcd for $C_{30}H_{34}BF_2N_3S_2Na^+$ $(M + Na)^+$ 572.21475, found 572.21466.

3. Results and discussion

3.1. Synthesis and structure of tBuazaBDPs

Synthetic routes of 3,5-*ditert*-butyl substituted aza-BODIPYs were outlined in Scheme 1a. 3,3-Dimethylbutan-2-one and aryl-containing aldehyde were ingeniously employed as the starting materials for the aldol condensation reaction. Nitromethane was added to produce nitro derivative **2**, which was dealed with ammonium acetate to provide the precursor **3** under the reflux condition. By the complexation with BF_3·

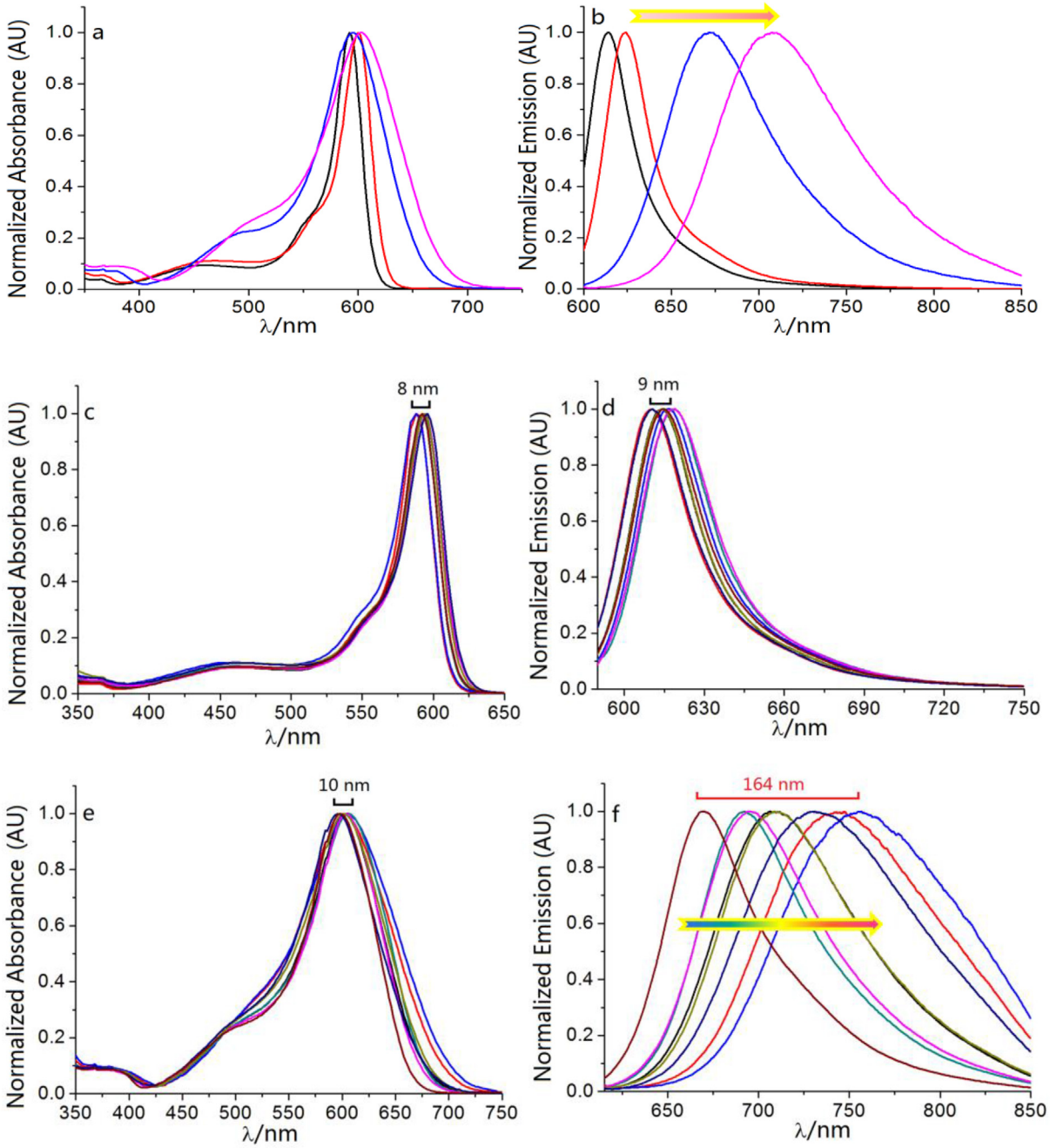

Fig. 2. (a) Normalized absorption and (b) emission spectra of **CF_3-tBuazaBDP** (black curve), ***C*N-tBuazaBDP** (red), **OMe-tBuazaBDP** (blue) and **SMe-tBuazaBDP** (pink) in CH_2Cl_2 solution at 298 K. (c) Normalized absorption and (d) emission spectra of **CF_3-tBuazaBDP**; (e) normalized absorption and (f) emission spectra of **SMe-tBuazaBDP** in various organic solutions (*n*-hexane, toluene, $CHCl_3$, CH_2Cl_2, THF, MeCN, DMF and DMSO) at 298 K.

Et_2O, the final dye **tBuazaBDP**s with 3,5-di-*tert*-butyl groups are obtained for the first time. **tBuazaBDP**s were clearly characterized by NMR spectroscopy and high resolution mass spectrometry. For example, by the identification of the ^1H NMR spectrum, two sets of the singlet distinct hydrogen signals for the –*t*Bu groups (δ = 1.55 (s, 18H) ppm) and the –SMe groups (δ = 2.54 (s, 6H) ppm) were observed respectively [49], which convincingly confirmed this structure of **SMe-tBuazaBDP**. Moreover, the molecular structure of **CN-tBuazaBDP** was indisputably demonstrated by the X-ray analysis of the prepared single crystal (Scheme 1c). The sp^3 hybridized boron center in **CN-tBuazaBDP** appeared in a distorted tetrahedron geometry with angles N2–B1–N3 of 106.7 (2)°, N2–B1–F2 of 106.5 (2)° and F1–B1–F2 of 111.4 (2)°, which seriously deviated from the ideal value of 119.5°. Consequently, the boron atom was found to severely upwarp from the core plane of ***C*N-tBuazaBDP**. Moreover, the C17–C16–C1–C2 dihedral angles were 22.9 (5)° and C14–C9–C6–C7 were −29.0 (4)° respectively, therefore two $–C_6H_4$(*p*-CN) groups at 1,7-sites in ***C*N-tBuazaBDP** located at both sides of the core and are non-coplanar (Scheme 1c-II), whereas two corresponding –Ph groups in **PhazaBDP** (Scheme 1b) nearly lie on the coplane of the aza-BODIPY core (Fig. S1) [39]. In short, the molecular structure of **tBuazaBDP** is more twisted than **PhazaBDP** [39].

3.2. Photophysical properties

Since 3,5-di-*tert*-butyl substituted **tBuazaBDP**s were synthesized for the first time, we are very curious to gain insight into their spectral properties. In stark comparison to **SMe-tBuazaBDP**, 3,5-diphenyl substituted aza-BODIPY **SMe-PhazaBDP** (Scheme 1b) is also prepared [50]. The *tert*-butyl substitution at 3,5-sites in **SMe-tBuazaBDP** ($\lambda_{abs}/\lambda_{em}$ = 602/708 nm) indeed undergoes the hypochromatic shift of the maxima absorption and emission by 70 and 27 nm respectively (Fig. 2a and b), comparing to those ($\lambda_{abs}/\lambda_{em}$ = 672/735 nm) of **SMe-PhazaBDP**. However, **SMe-tBuazaBDP** possesses ultra-large Stokes shift (106 nm) and still has the NIR emission wavelength (Fig. 2a and b). Furthermore, the introduction of the push-pull electron groups at 1,7-sites in **R-tBuazaBDP**s (Scheme 1a) results in the bathochromic shift (4–14 nm) of absorption in CH_2Cl_2 solution (Fig. 2a and Table 1), compared with that (λ_{abs} = 588 nm) of **H-tBuazaBDP** (R = H, Scheme 1a) [51]. It is noteworthy that the Stokes shift slightly decreased (22 nm for **CF_3-tBuazaBDP**, 24 nm for ***C*N-tBuazaBDP**) by the introduction of the electron-withdrawing groups, comparing to that (25 nm) of **H-tBuazaBDP**, although the absorption and emission spectra showed bathochromic shift simultaneously. Nevertheless, wide full width at half maximum (FWHM: 85 nm) of **SMe-tBuazaBDP** is broader than that (33 nm) of **CF_3-tBuazaBDP**. Moreover, half width of the fluorescence band of **SMe-tBuazaBDP** is even broader and about three times than that of **CF_3-tBuazaBDP**. The molar extinction coefficients increase slightly, along with the change of the pull or push electron groups. Especially, we were surprised to discover that the introduction of the –SMe group led to low fluorescence quantum yield (Φ_f = 0.05), compared with other **tBuazaBDP**s. In sharp contrast to **Rev-SMe-tBuazaBDP** [52] with the group exchange at 1,7 and 3,5-sites (Scheme 1b) from **SMe-tBuazaBDP**, although the maxima emission between **Rev-SMe-tBuazaBDP** (λ_{em} = 713 nm) and **SMe-tBuazaBDP** (λ_{em} = 708 nm) could indeed be comparable, the maximum absorption of **SMe-tBuazaBDP** (λ_{abs} = 602 nm) is obviously hypochromatic shift relative to that (λ_{abs} = 666 nm) of **Rev-SMe-tBuazaBDP**, so **SMe-tBuazaBDP** shows a larger Stokes shift (106 nm) than that (47 nm) of **Rev-SMe-tBuazaBDP**. Therefore, a breakthrough of ultra-large Stokes shift was found in the spectral properties of 3,5-di-*tert*-butyl-substituted aza-BODIPYs in this work.

Table 1
Spectral data of aza-BODIPYs in CH_2Cl_2 solution at 298 K.

Aza-BODIPY	$\lambda_{abs}/\lambda_{em}$ (nm)	Stokes shift (nm)	FWHM (nm)	ε [M^{-1} cm^{-1}]	Φ_f
H-tBuazaBDP	588/613	25	31	74,000	0.12
CF_3-tBuazaBDP	592/614	22	29	73,500	0.12
***C*N-tBuazaBDP**	600/624	24	33	73,000	0.11
OMe-tBuazaBDP	596/672	76	71	75,500	0.13
SMe-tBuazaBDP	602/708	106	85	76,000	0.05
SMe-PhazaBDP	672/735	63	75	80,000	0.07
Rev-SMe-tBuazaBDP	666/713	47	73	85,000	0.04

In order to further deeply gain insight into the influence of the electron donating/withdrawing modifications on the spectral properties, we investigated the solvent effects of **H-tBuazaBDP**, **CF_3-tBuazaBDP** and **SMe-tBuazaBDP**. As shown in Fig. 2c and d and Table S1, the solvent effect between **H-tBuazaBDP** and **CF_3-tBuazaBDP** is not significantly different. For instance, the absorption and emission maxima of **CF_3-tBuazaBDP** in nonpolar solvent *n*-hexane locate at 588 and 610 nm, respectively. In the large polar solvent DMSO, a slight red-shift was monitored at 596 and 619 nm for absorption and emission maxima, while molar extinction coefficients and Stokes shifts were similar in different solvents. Different from **CF_3-tBuazaBDP**, the solvent effect on **SMe-tBuazaBDP** was comparatively evident. As shown in Fig. 2e and f, although there is a slight difference in absorption spectra in different solvents, the emission spectra of **SMe-tBuazaBDP** show dramatic discrepancy. In nonpolar solvent *n*-hexane, the absorption and emission maxima of **SMe-tBuazaBDP** are 598 and 670 nm, respectively. However, in the large polar solution DMSO, although the absorption only red-shifted by 6 nm–604 nm, the maximum emission was unexpectedly red-shifted to 756 nm and Stokes shift spectacularly reached 152 nm. This is probably due to the synergic action of TICT effect and the release energy by free rotation of the −*t*Bu group at 3,5-sites in **SMe-tBuazaBDP** (see the following Fig. 3a). Since the large Stokes shift can improve the sensitivity of photochemical application and avoid the self-quenching of the excited and scattered light affiliated measurement error, Peng et al. synthesized the heptamethine cyanine dyes by introducing alkylamino groups with large Stokes shift (140 nm), which is facilitated for optical applications such as fluorescent labeling [53]. Hence, **SMe-tBuazaBDP** with the ultra-large Stokes shift is highly desirable for a photothermal therapy. FWHM of **SMe-tBuazaBDP** become wider with the increase of solvent polarity, but the light-harvesting ability has not change significantly in different solvents. It is worth mentioning that in DMF and DMSO solution, the fluorescence quantum yield of **SMe-tBuazaBDP** is significantly reduced (Φ_f = 0.02) (Table S1).

3.3. Theoretical calculations

To further rationalize the special optical properties of **SMe-tBuazaBDP**, theoretical simulations are conducted based on DFT and TDDFT methods, and **SMe-PhazaBDP** is selected to serve as a scrupulously comparative molecule (Scheme 1b) [50]. The calculated absorption spectra of **SMe-tBuazaBDP** and **SMe-PhazaBDP** are displayed in Fig. S3. The agreement between theoretical and experimental data confirms the current calculation level and the reliability of the theoretical results. To figure out the causality of the large Stokes shift of **SMe-tBuazaBDP**, the frontier molecular orbital analysis is carried out. The primary absorption and emission peaks of **SMe-tBuazaBDP** both correspond to the S_0–S_1 transition (Table S4-6), which is composed of the transition between the highest occupied molecular orbital (HOMO) and the lowest unoccupied molecular orbital (LUMO). As shown in Fig. S4, the electron density of HOMO mainly distributes on the non-*t*Bu groups, whereas the LUMO mainly concentrates on the BODIPY core. The different location of HOMO and LUMO results in the transition between them, undergoing a TICT process, which usually leads to a weak fluorescence and an ultra-large Stokes shift [54,55]. Moreover, the rotational process between **SMe-tBuazaBDP** and **SMe-PhazaBDP** are compared, as shown in Fig. 3a. The scan process covers 180° rotation divided into 6 steps. **SMe-tBuazaBDP** has smaller energy barriers (2.8 kcal/mol) along the rotation of the –*t*Bu group, comparing to that (3.2 kcal/mol) of the –Ph

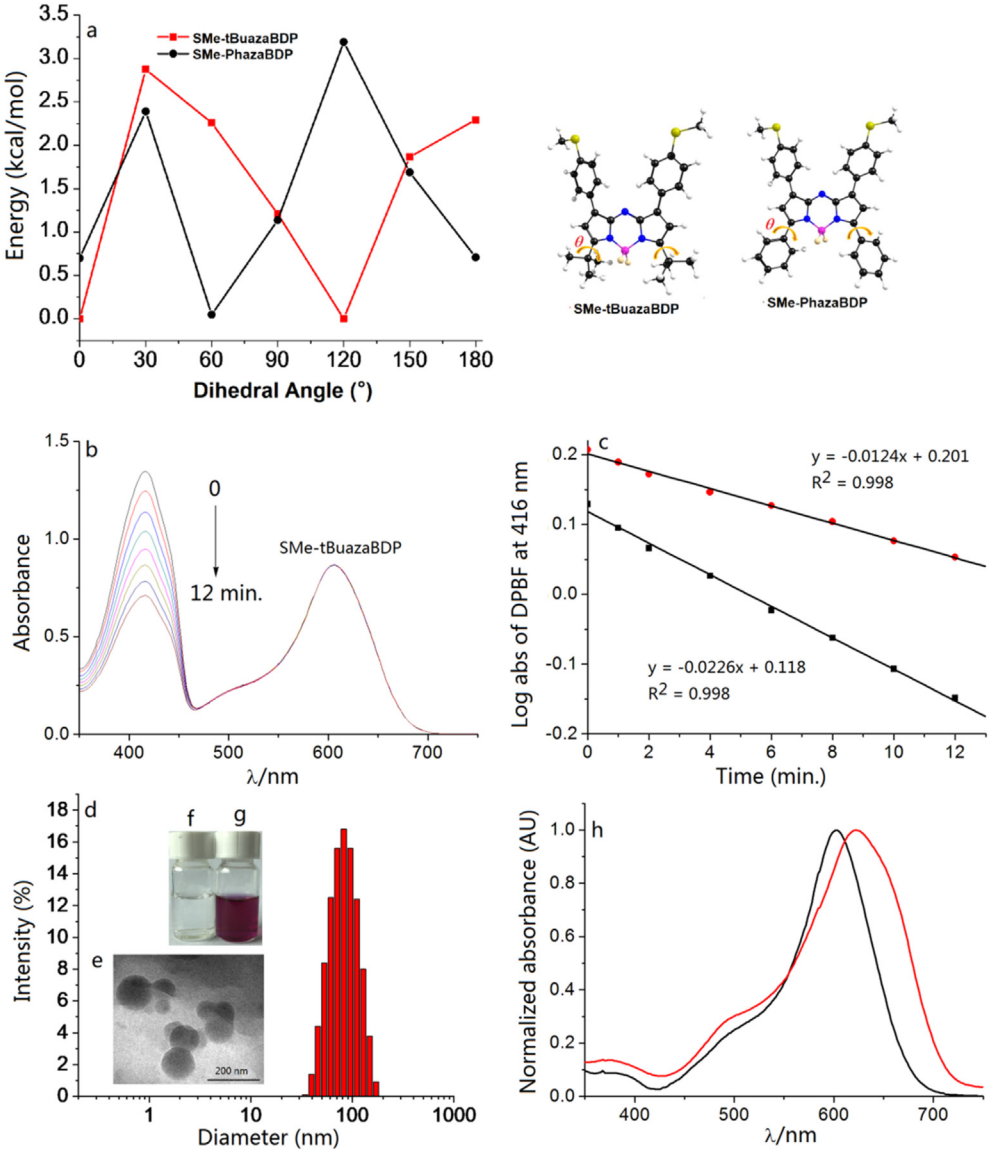

Fig. 3. (a) Potential energy curves of **SMe-tBuazaBDP** and **SMe-PhazaBDP** along the rotation of the substituted group. (b) Absorption curve of **SMe-tBuazaBDP** and DPBF in toluene with time under light irradiation; (c) Comparison of absorption decline rate of DPBF in **SMe-tBuazaBDP** ($S = -0.0226$) and **CF_3-tBuazaBDP** ($S = -0.0124$) with time. T = 298 K. (d) DLS and (e) TEM of SMe-tBuazaBDP NPs in aqueous solution; (f) Photo of pure water and (g) Photo of SMe-tBuazaBDP NPs in water. (h) Absorption spectra of SMe-tBuazaBDP (black curve) in CH_2Cl_2 and SMe-tBuazaBDP NPs (red) in aqueous solution.

group in **SMe-PhazaBDP**. Such small energy barriers promise their *free* rotation in solution [56,57], which may cause more system energy released through non-radiative decay. Hence, the ultra-large Stokes shift of **SMe-tBuazaBDP** may attribute to the TICT and rotational energy release of the –*t*Bu groups.

3.4. Singlet oxygen generation ability

To further investigate the effect of the electron donating/withdrawing group modification on the excited state release energy of **CF_3-tBuazaBDP** and **SMe-tBuazaBDP**, 1,3-diphenlisobenzofuran (DPBF), the singlet oxygen ($^1O_2$) capture agent, is applied to indicate $^1O_2$ production in toluene solution. Once the solution is irradiated by the light, the absorption of DPBF at 416 nm gradually decreases with the increase of light radiation time, while the absorption maximum of **SMe-tBuazaBDP** did not change, indicating that **SMe-tBuazaBDP** has a favorable photostability (Fig. 3b). Then we also investigated the DPBF decline extent of **CF_3-tBuazaBDP** under the same conditions. **SMe-tBuazaBDP** was found to possess a relatively faster reduction efficiency of DPBF ($S = -0.0226$), compared with that ($S = -0.0124$) of **CF_3-tBuazaBDP** (Fig. 3c). Their singlet oxygen yields are low and calculated to be 8.1% for **SMe-tBuazaBDP** and 4.4% for **CF_3-tBuazaBDP**, respectively [58]. In terms of the calculation formula, one can find that ISC (k_{ISC}) rate is closely related to singlet-triplet energy differences (ΔE_{st}) [59–61]. So, to estimate the difficulty of the ISC, the first ten lowest-lying singlet and triplet transitions of **SMe-tBuazaBDP** have been calculated, as listed in Table S4. Obviously, the energy gap ΔE_{st} between S_1 and T_1 state is about 1 eV, which is not a favorable energy difference for ISC [59–61]. In short, **SMe-tBuazaBDP** exhibits a weak ISC effect.

3.5. Synthesis and characterization of SMe-tBuazaBDP NPs

The low conversion efficiency for two above described pathways from the excited state to the ground state urges us to investigate the third pathway, that is, non-radiative decay. Since the rotation of the bulk groups (such as $–CF_3$, –*t*Bu) for non-radiative decay can promote the heat energy conversion [39,45], we next investigated the photothermal conversion effect of **SMe-tBuazaBDP**. First, to improve the water solubility and biocompatibility of **SMe-tBuazaBDP** for better application in photo-imaging and therapy in biological systems, **SMe-tBuazaBDP** and

polymer materials DSPE-PEG_{2000} were self-assembled into dye nanoparticles (**SMe-tBuazaBDP** NPs) [62,63]. Transmission electron microscopy (TEM) photograph demonstrated the spherical morphology of the nanoparticles, and their sizes were less than 110 nm (Fig. 3d and e). Dynamic light scattering (DLS) of **SMe-tBuazaBDP** NPs showed a suitable hydrodynamic diameter (30–110 nm) in Fig. 3d, and the average hydrodynamic diameter and the polydispersity index (PDI) of **SMe-tBuazaBDP** NPs were about 85.5 nm and 0.31, respectively [64,65]. After being placed in aqueous solution for two weeks, no precipitate was observed and the particle size did not change significantly, suggesting that the prepared nanoparticles are stable (Fig. 3f and g). Due to the bulky *tert*-butyl substituents as spacers in the aggregation (Fig. S5), the absorption of **SMe-tBuazaBDP** NPs in aqueous solution is red-shifted (λ_{abs} = 624 nm) and the peak becomes wider (Table S7), covering from 450 to 750 nm, comparing to that (λ_{abs} = 602 nm) of **SMe-tBuazaBDP** in organic solvent CH_2Cl_2 (Fig. 3h).

3.6. Photothermal conversion performance

As depicted in Fig. 4, the temperature of the solution increased significantly under the light irradiation of **SMe-tBuazaBDP** NPs in the aqueous solution. For instance, after 1 min light irradiation, the solution temperature rapidly increased by 11.3 °C and its temperature even reached 56.0 °C after only 4 min light irradiation (Fig. 4a), achieving strong light absorption ability and thermal energy release properties. Since hyperthermia (above 42 °C) generated by nanomaterials under laser irradiation could effectively destruct cancer cells [20,21,66], **SMe-tBuazaBDP** NPs are consequently suitable for hyperthermia. Next, we further monitored the temperature enhancement at different concentrations (20, 40 and 80 μM) of **SMe-tBuazaBDP** NPs and different optical power densities (0.1, 0.2 and 0.3 W cm^{-2}) (Fig. 4b and c). As shown in Fig. 4b and c, temperature promotion is intimately dependent on concentration and power density. Higher concentration and stronger power density contribute to better thermal conversion effect. The temperature change under natural cooling phase after 10 min light radiation was investigated. In Fig. 4d, the solution temperature in the heating phase achieved a rapid heating effect for 5 min, and the temperature will slowly rise to the peak after 5 min light radiation. Once stopping the radiation, the temperature of the solution cooled rapidly to near room temperature after 5 min, and the cooling effect was not significant for the next 5 min. Hence, light radiation for 10 min and natural cooling for 10 min were selected as one cycle to inspect three heating-cooling cycles testing. As can be seen from Fig. 4d, the temperature changes during the heating-cooling cycle of each group are almost the same, suggesting that **SMe-tBuazaBDP** NPs have excellent photothermal stability and can be applied for the photothermal therapy for multiple cycles. Furthermore, to investigate the photothermal conversion efficiency, the associated time constant obtained by mapping the cooling time and driving force temperature was brought into the reported formula for calculating the photothermal conversion efficiency. The photothermal conversion efficiency of **SMe-tBuazaBDP** NPs was calculated to be 49.3% (Fig. 4e and f), which is near to the highest one (50.5%) in aza-BODIPY-based system [67,68]. Moreover, this is obviously higher than that (45%) of the contrastive dye **SMe-PhazaBDP** [50] or those of the classical photothermal agents, such as ICG (27.9%) [17], indicating that this strategy of the 3,5-*tert*-butyl substitution in aza-BODIPY system is an effective way to enhance the photothermal conversion.

3.7. Cytotoxicity assay and PTT performance in vitro

To determine the suitable time of light radiation to **SMe-tBuazaBDP** NPs, we performed CCK8 assay with human colon cancer (SW-620) cells and gastric cancer (SGC-7901) cells. As is shown in Fig. 5a, the inhibition of cell viability was significant when the laser radiation time exceeded

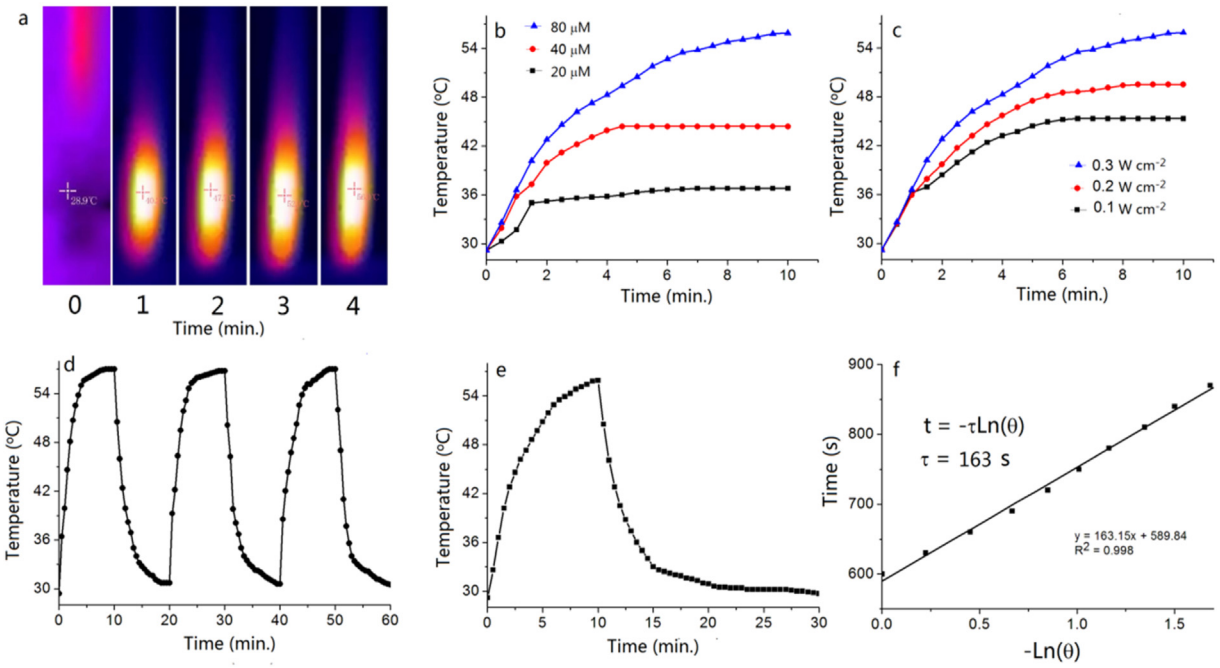

Fig. 4. a) Photothermal images of **SMe-tBuazaBDP** NPs in aqueous solution under 635 nm laser irradiation (0.3 W cm^{-2}, 0–4 min, 29–56 °C); b) Photothermal conversion of **SMe-tBuazaBDP** NPs at different concentrations (20, 40, 80 μM) under laser irradiation (0.3 W cm^{-2}); c) Photothermal conversion of **SMe-tBuazaBDP** NPs (80 μM) under laser irradiation with different power density (0.1, 0.2, 0.3 W cm^{-2}); d) Photothermal stability study during three circles of heating-cooling processes; e) Photothermal curve of **SMe-tBuazaBDP** NPs in aqueous solutions (80 μM) under irradiation (0.3 W cm^{-2}) and after naturally cooling to room temperature; f) Linear fitting of $-\mathrm{Ln}\theta$ and time.

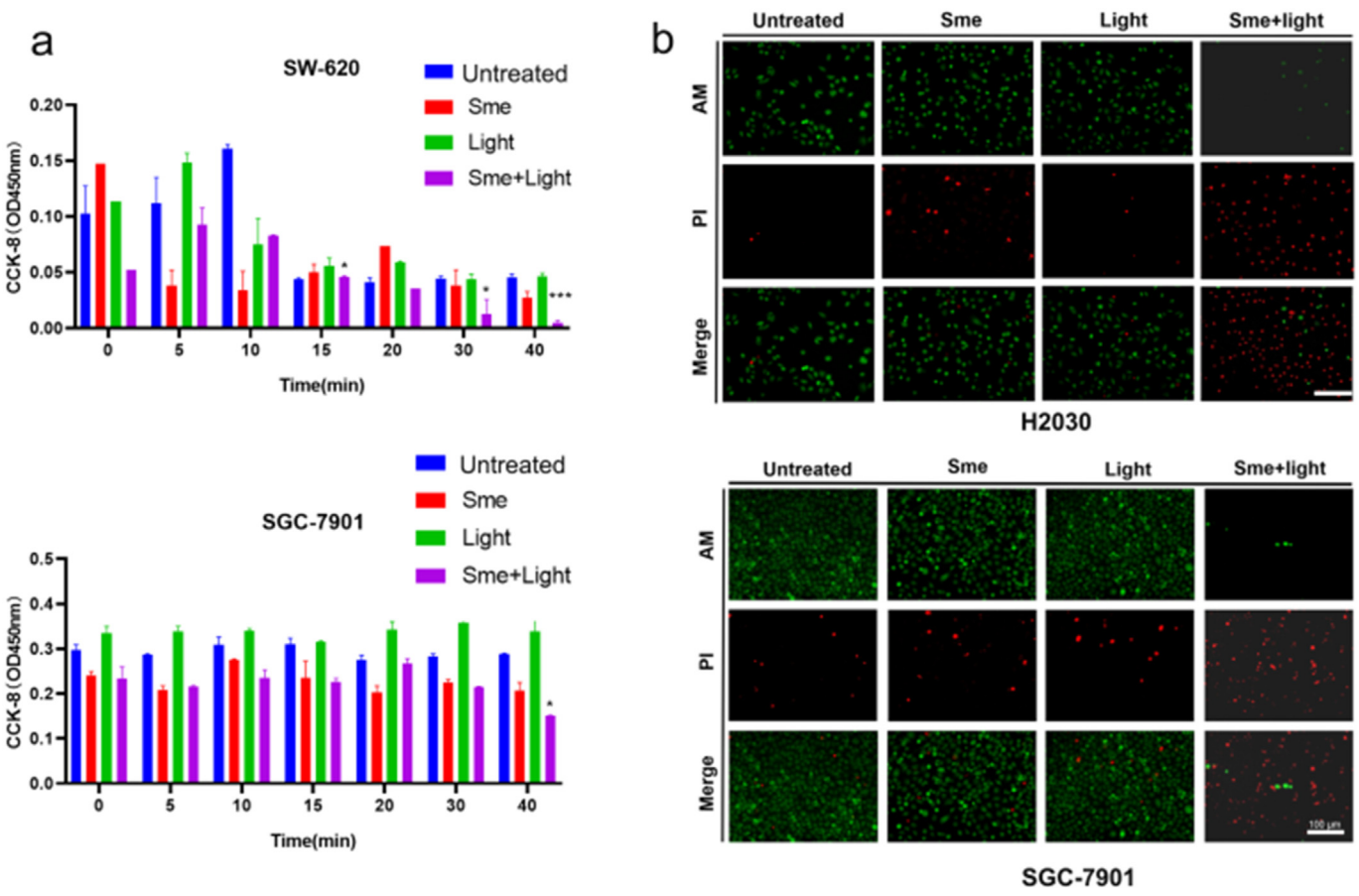

Fig. 5. a) Cell viability was analyzed by CCK-8 assay in SW-620 cells and SGC-7901 cells after different treatment under different illumination time. *, $p < 0.05$; **, $p < 0.01$; ***, $p < 0.001$; ****, $p < 0.0001$. Compared with other treatment groups, the cell viability of the group under treatment with **SMe-tBuazaBDP** NPs (30 μM) and light irradiation (0.2 W cm^{-2}) decreased significantly when the illumination time was more than 15 min. b) Fluorescence images of calcine AM and PI co-stained NCI–H2030 cells and SGC-7901 cells after incubation with 30 μM **SMe-tBuazaBDP** NPs with or without 635 nm laser irradiation (0.2 W cm^{-2}) for 20 min, respectively. Scale bar: 100 μm. For clarity, **SMe-tBuazaBDP** NPs is abbreviated as Sme in Fig. 5.

15 min, indicating that **SMe-tBuazaBDP** NPs possess low dark cytotoxicity and high phototoxicity [17]. Therefore, the laser radiation time of 20 min was selected as the condition of the subsequent experiment to continue to investigate the phototherapeutic performance of **SMe-tBuazaBDP** NPs. Then, to further verify the inhibitory effect of **SMe-tBuazaBDP** NPs with laser radiation time of 20 min on various cancer cell viability, we performed live-dead cell staining by using calcine AM (green) and propidium iodide (red) dyes. Human lung cancer (NCI–H2030) cells also were used for the experiment. As expected, **SMe-tBuazaBDP** NPs induced death of NCI–H2030 cells and SGC-7901 cells after laser radiation (0.2 W cm^{-2}, 20 min), as shown by the significant red fluorescence, while only light or **SMe-tBuazaBDP** NPs groups demonstrated apparent green fluorescence, which was the same as the control group (Fig. 5b). The results suggested that **SMe-tBuazaBDP** NPs could lead to the death of cancer cells through the photothermal effect.

3.8. Determination on cell death mechanism

Since apoptosis and necrosis are well-known to be two important modes during cell death in PTT [47,48], therefore the cell death mechanism induced by **SMe-tBuazaBDP** NPs was herein investigated. To determine whether **SMe-tBuazaBDP** NPs with laser radiation has effect on the cycle and apoptosis of cancer cells, we first performed flow cytometry with SGC-7901 cells. As shown in Fig. 6a, compared with other groups, cells treated with **SMe-tBuazaBDP** NPs and laser irradiation group showed an increase in G2 phase and a decrease in S phase, which caused G0/G1 arrest, suggesting that **SMe-tBuazaBDP** NPs blocked cell cycle progression and inhibited proliferation of cancer cells via laser radiation (Fig. 6a). Moreover, Fig. 6b showed that the percentage of apoptotic cells increased from 3.9% (blank control) to 30.5% after treatment with **SMe-tBuazaBDP** NPs and laser radiation, while SGC-7901 cells treated with **SMe-tBuazaBDP** NPs or light irradiation displayed lower apoptosis rate (18.4%, 4.6%), indicating the efficient apoptosis-inducing capacity of **SMe-tBuazaBDP** NPs to cancer cells. Next, we further performed RT-qPCR and western blot to verify the effects of **SMe-tBuazaBDP** NPs with laser radiation on apoptosis and cell cycle at mRNA and protein levels with various factors related to the regulation of cell cycle and apoptosis (Fig. 6c and d). Herein, Bcl2 is a negative regulator of apoptosis, while Bax is a positive regulator of apoptosis (Fig. 6c). In the group treated with **SMe-tBuazaBDP** NPs and light irradiation, the mRNA level and protein level of Bcl2 decreased significantly compared with other groups, while the mRNA level of Bax increased significantly, which further proved that the photothermal effect of the **SMe-tBuazaBDP** NPs could induce cancer cell apoptosis (Fig. 6c). Meanwhile, as shown in Fig. 6d, the decrease of expression level of *C*-myc and cyclin-D1 showed that treatment with **SMe-tBuazaBDP** NPs and light irradiation induced cell cycle arrest, blocked cancer cell cycle and inhibited cell proliferation. These results demonstrated strong consistency with the Calcein AM/PI results, suggesting that

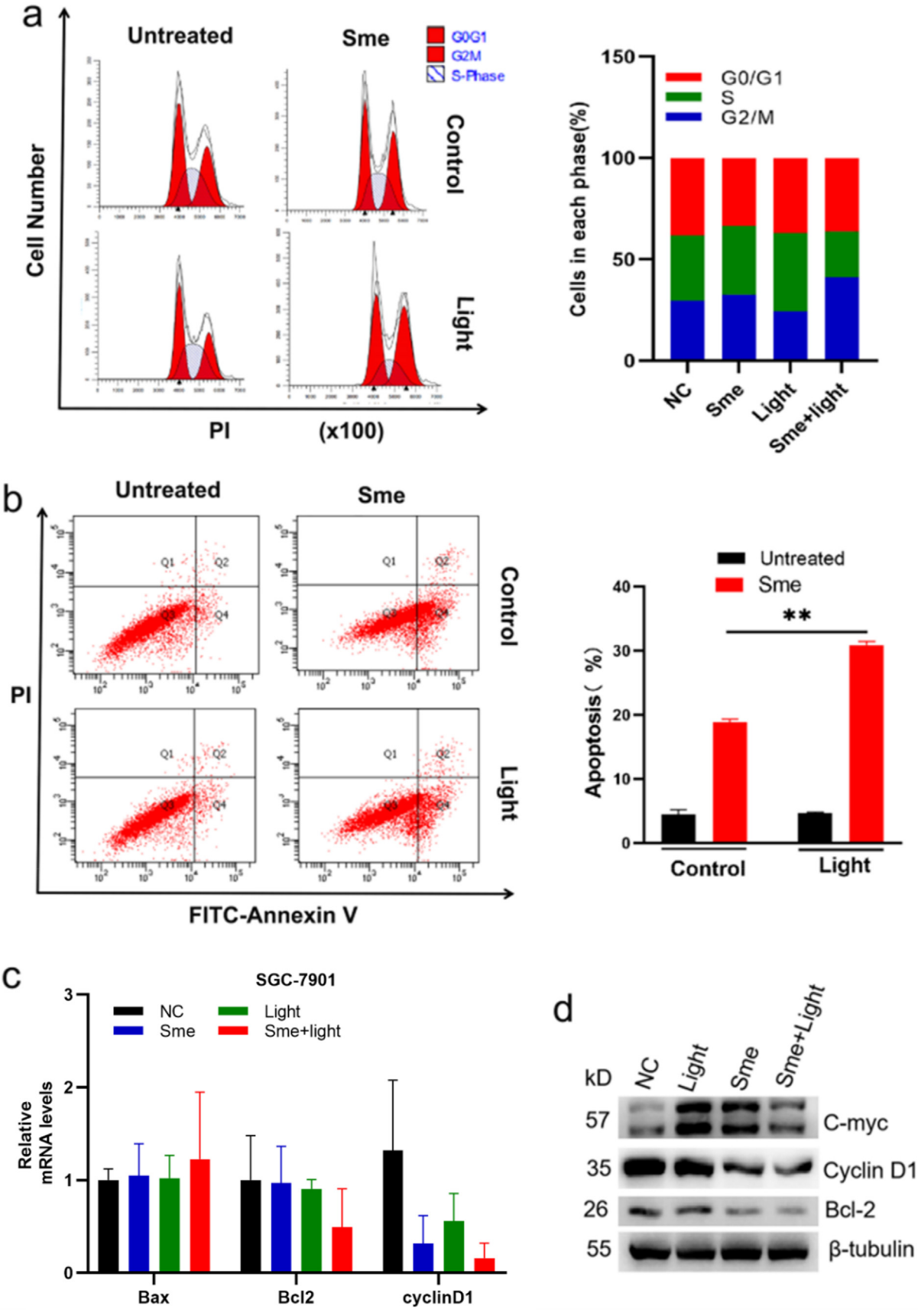

(caption on next page)

Fig. 6. a) Cell cycle analysis using flow cytometry in SGC-7901 cells after treatment with **SMe-tBuazaBDP** NPs (30 μM) alone, light alone or their combination. Light irradiation (0.2 W cm^{-2}, 20 min) was conducted after cells were incubated with **SMe-tBuazaBDP** NPs. b) Apoptosis analysis using flow cytometry toward SGC-7901 cells after treatment with **SMe-tBuazaBDP** NPs (30 μM) alone, light alone or their combination. Light irradiation (0.2 W cm^{-2}, 20 min) was conducted after cells were incubated with **SMe-tBuazaBDP**. **SMe-tBuazaBDP** NPs treatment with laser irradiation was shown to induce more apoptosis. *, $p < 0.05$; **, $p < 0.01$; ***, $p < 0.001$; ****, $p < 0.0001$. c) mRNA expression level related to regulation of cell cycle (cyclin-D1) and apoptosis (Bcl-2, Bax) were evaluated using RT-qPCR in SGC-7901 cells after treatment with **SMe-tBuazaBDP** NPs (30 μM) alone, light (0.2 W cm^{-2}, 20 min) alone or their combination. d) The expression level of protein related to regulation of cell cycle (cyclin-D1), cell proliferation (*C*-myc) and apoptosis (Bcl-2) were evaluated by western blot in NCI–H2030 cells after treatment with **SMe-tBuazaBDP** NPs (30 μM) alone, light (0.2 W cm^{-2}, 20 min) alone or their combination. For clarity, **SMe-tBuazaBDP** NPs is abbreviated as Sme in Fig. 6.

SMe-tBuazaBDP NPs with low laser radiation effectively blocked cancer cell cycle, inhibited cancer cell proliferation and induced cancer cell apoptosis. Therefore, **SMe-tBuazaBDP** NPs provide great possibilities as a cancer photothermal agent.

4. Conclusion

In summary, we successfully synthesized a series of innovative dyes, 3,5-di-*tert*-butyl-substituted **tBuazaBDP**s for the first time. Based on the X-ray analysis of the prepared single crystal ***C*N-tBuazaBDP**, the molecular structure of **tBuazaBDP** is twisted. **SMe-tBuazaBDP** has the ultra-large Stokes shift in aza-BODIPY system, which may attribute to the TICT and the rotational energy release of the −*t*Bu groups based on the experiment and theoretical calculation. Although the barrier-free rotors of the distal −*t*Bu groups in **SMe-tBuazaBDP** results in low fluorescence quantum yield, its photothermal conversion efficiency ($\eta = 49.3\%$) is obviously enhanced. **SMe-tBuazaBDP** NPs realized the photo-toxicity to effectively block cancer cell cycle, inhibit cancer cell proliferation and induce cancer cell apoptosis by the optical radiation driven for photothermal therapy. The strategy of "direct attachment of −*t*Bu groups to aza-BODIPY core at 3,5-sites" provides a meaning idea for opening a new platform for the future design of PTAs.

Credit author statement

R. L, X. J. carried out the synthetic work and analytical characterization, including the crystallographic studies. **J. R, Z. W, H. W, S. Z**. performed the experiments on cell apoptosis and fluorescence imaging. **M. L**. carried out the computational studies. **D. Z**. assisted with data analysis. **D. Z, J. D, X. J, G. W**. wrote the manuscript. **X. J**. supervised the research. All authors reviewed and approved the manuscript.

Declaration of Competing Interest

The authors declare that they have no known competing financial interests or personal relationships that could have appeared to influence the work reported in this paper.

Data availability

Data will be made available on request.

Acknowledgements ((optional))

This work was supported by the National Natural Science Foundation of China (22078201, U1908202), "Chunhui Program" cooperative research project of Education Ministry, Natural Science Foundation of Liaoning (2021NLTS1206), serving local project of Education Department of Liaoning Province (LZ2020005), Liaoning & Shenyang Key Laboratory of Functional Dye and Pigment (2021JH13/10200018, 21-104-0-23) and the Distinguished Professor Project Liaoning Province (20183532).

Appendix A. Supplementary data

Supplementary data to this article can be found online at https://doi.org/10.1016/j.mtbio.2022.100446.

References

[1] L. Goodman, M. Wintrobe, W. Dameshek, M. Goodman, A. Gilman, M. McLennan, Nitrogen mustard therapy, use of methyl-bis (beta-chloroethyl) amine hydrochloride and tris (beta-chloroethyl) amine hydrochloride for Hodgkin's disease, lymphosarcoma, leukemia and certain allied and miscellaneous disorders, JAMA 132 (1946) 126–132.
[2] Y. Yang, X. Liu, W. Ma, Q. Xu, G. Chen, Y. Wang, H. Xiao, N. Li, X.-J. Liang, M. Yu, Z. Yu, Light-activatable liposomes for repetitive on-demand drug release and immunopotentiation in hypoxic tumor therapy, Biomaterials 265 (2021), 120456.
[3] L. Yu, Z. Wang, Z. Mo, B. Zou, Y. Yang, R. Sun, W. Ma, M. Yu, S. Zhang, Z. Yu, Synergetic delivery of triptolide and Ce6 with light-activatable liposomes for efficient hepatocellular carcinoma therapy, Acta Pharm. Sin. B 11 (2021) 2004–2015.
[4] G. Chen, Y. Yang, Q. Xu, M. Ling, H. Lin, W. Ma, R. Sun, Y. Xu, X. Liu, N. Li, Z. Yu, M. Yu, Self-amplification of tumor oxidative stress with degradable metallic complexes for synergistic cascade tumor therapy, Nano Lett. 20 (2020) 8141–8150.
[5] Y. Yang, Y. Yu, H. Chen, X. Meng, W. Ma, M. Yu, Z. Li, C. Li, H. Liu, X. Zhang, H. Xiao, Z. Yu, Illuminating platinum transportation while maximizing therapeutic efficacy by gold nanoclusters via simultaneous near-infrared-I/II imaging and glutathione scavenging, ACS Nano 14 (2020) 13536–13547.
[6] Y. Sun, Y. Liang, W. Dai, B. He, H. Zhang, X. Wang, J. Wang, S. Huan, Q. Zhang, Peptide-drug conjugate-based nanocombination actualizes breast cancer treatment by maytansinoid and photothermia with the assistance of fluorescent and photoacoustic images, Nano Lett. 19 (2019) 3229–3237.
[7] G. Yim, S. Kang, Y.J. Kim, Y.K. Kim, D.H. Min, H. Jang, Hydrothermal galvanic-replacement-tethered Synthesis of Ir-Ag-IrO_2 nanoplates for computed tomography-guided multiwavelength potent thermodynamic cancer therapy, ACS Nano 13 (2019) 3434–3447.
[8] H. Huang, S. Baneerjee, K. Qiu, P. Zhang, O. Blancque, T. Malcomson, M.J. Paterson, G.J. Clarkson, M. Staniforth, V.G. Stavros, G. Gasser, H. Chao, P.J. Sadler, Targeted photoredox catalysis in cancer cells, Nat. Chem. 11 (2019) 1041–1048.
[9] W. Fan, P. Huang, X. Chen, Overcoming the Achilles' heel of photodynamic therapy, Chem. Soc. Rev. 45 (2016) 6488–6519.
[10] W. Fan, B. Yung, P. Huang, X. Chen, Nanotechnology for multimodal synergistic cancer therapy, Chem. Rev. 117 (2017) 13566–13638.
[11] X. Zhao, C.X. Yang, L.G. Chen, X.P. Yan, Dual-stimuli responsive and reversibly activatable theranostic nanoprobe for precision tumor-targeting and fluorescence-guided photothermal therapy, Nat. Commun. 8 (2017), 14998.
[12] Z. Zhou, J. Song, L. Nie, X. Chen, Reactive oxygen species generating systems meeting challenges of photodynamic cancer therapy, Chem. Soc. Rev. 45 (2016) 6597–6626.
[13] M. Zhao, Y. Xu, M. Xie, L. Zou, Z. Wang, S. Liu, Q. Zhao, Halogenated aza-BODIPY for imaging-guided synergistic photodynamic and photothermal tumor therapy, Adv. Healthcare Mater. (2018), 1800606.
[14] W. Fan, P. Huang, X. Chen, Overcoming the Achilles' heel of photodynamic therapy, Chem. Soc. Rev. 45 (2016) 6488–6519.
[15] X. Zhao, S. Long, M. Li, J. Cao, Y. Li, L. Gou, W. Sun, J. Du, J. Fan, X. Peng, Oxygen-dependent regulation of excited-state deactivation process of rational photosensitizer for smart phototherapy, J. Am. Chem. Soc. 142 (2020) 1510–1517.
[16] H.S. Jung, J.H. Lee, K. Kim, S. Koo, P. Verwilst, J.L. Sessler, C. Kang, J.S. Kim, A mitochondria-targeted cryptocyanine-based photothermogenic photosensitizer, J. Am. Chem. Soc. 139 (2017) 9972–9978.
[17] Y. Liu, P. Bhattarai, Z. Dai, X. Chen, Photothermal therapy and photoacoustic imaging via nanotheranostics in fighting cancer, Chem. Soc. Rev. 48 (2019) 2053–2108.
[18] K. Shimomura, H. Kai, Y. Nakamura, Y. Hong, S. Mori, K. Miki, K. Ohe, Y. Notsuka, Y. Yamaoka, M. Ishida, D. Kim, H. Furuta, Bis-metal complexes of doubly N-confused dioxohexaphyrins as potential near-infrared-II photoacoustic dyes, J. Am. Chem. Soc. 142 (2020) 4429–4437.

[19] M. Zhao, Y. Xu, M. Xie, L. Zou, Z. Wang, S. Liu, Q. Zhao, Halogenated aza-BODIPY for imaging-guided synergistic photodynamic and photothermal tumor therapy, Adv. Healthcare Mater. (2018), 1800606.

[20] Van-Nghia Nguyen, Zhao Zheng, Ben Zhong Tang, Juyoung Yoon, Organic photosensitizers for antimicrobial phototherapy, Chem. Soc. Rev. 51 (2022) 3324–3340.

[21] G. Gao, Y.W. Jiang, W. Sun, Y. Guo, H.R. Jia, X.W. Yu, G.Y. Pan, F.G. Wu, Small 15 (2019), 1900501.

[22] B. Tang, W.L. Li, Y. Chang, B. Yuan, Y. Wu, M.T. Zhang, J.F. Xu, J. Li, X. Zhang, A supramolecular radical dimer: high-efficiency NIR-II photothermal conversion and therapy, Angew. Chem. Int. Ed. 58 (2019) 15526–15531.

[23] X. Ding, C.H. Liow, M. Zhang, R. Huang, C. Li, H. Shen, M. Liu, Y. Zou, N. Gao, Z. Zhang, Y. Li, Q. Wang, S. Li, J. Jiang, Surface plasmon resonance enhanced light absorption and photothermal therapy in the second near-infrared window, J. Am. Chem. Soc. 136 (2014) 15684–15693.

[24] C. Wu, X. Huang, Y. Tang, W. Xiao, L. Sun, J. Shao, X. Dong, Pyrrolopyrrole aza-BODIPY near-infrared photosensitizer for dual-mode im-aging-guided photothermal cancer therapy, Chem. Commun. 55 (2019) 790–793.

[25] Y. Tang, L. Xue, Q. Yu, D. Chen, Z. Cheng, W. Wang, J. Shao, X. Dong, Smart aza-BODIPY photosensitizer for tumor microenvironment-enhanced cancer phototherapy, ACS Appl. Bio Mater. 2 (2019) 5888–5897.

[26] A. Jablonski, Über den Mechanismus der Photolumineszenz von Farbstoffphosphoren, Z. Phys. 94 (1935) 38–46.

[27] V.N. Nguyen, J. Ha, M. Cho, H. Li, K. Swamy, J. Yoon, Recent developments of BODIPY-based colorimetric and fluorescent probes for the detection of reactive oxygen/nitrogen species and cancer diagnosis, Coord. Chem. Rev. 439 (2021), 213936.

[28] H. Zhang, J. Liu, Y. Sun, M. Liu, W. Guo, Carbon-dipyrromethenes: bright cationic fluorescent dyes and potential application in revealing cellular trafficking of mitochondrial glutathione conjugates, A fluorogenic $ONOO^-$-Triggered carbon monoxide donor for mitigating brain ischemic damage, J. Am. Chem. Soc. 142 (2020) 17069–17078.

[29] L. Xing, B. Wang, J. Li, X. Guo, X. Lu, X. Chen, H. Sun, Z. Sun, X. Luo, S. Qi, X. Qian, Y. Yang, A fluorogenic $ONOO^-$-Triggered carbon monoxide donor for mitigating brain ischemic damage, J. Am. Chem. Soc. 144 (2022) 2114–2119.

[30] T. Fang, X.-D. Jiang, C. Sun, Q. Li, BODIPY-based naked-eye fluorescent on-off probe with high selectivity for H_2S based on thiolysis of dinitrophenyl ether, Sens. Actuators B Chem. 290 (2019) 551–557.

[31] Y. Ge, F.D. O'Shea, Chem. Azadipyrromethenes: from traditional dye chemistry to leading edge applications, Soc. Rev. 45 (2016) 3846–3864.

[32] Z. Shi, X. Han, W. Hu, H. Bai, B. Peng, L. Ji, Q. Fan, L. Li, W. Huang, Bioapplications of small molecule Aza-BODIPY: from rational structural design to in vivo investigations, Chem. Soc. Rev. 49 (2020) 7533–7567.

[33] Q. Tang, W. Xiao, C. Huang, W. Si, J. Shao, W. Huang, P. Chen, Q. Zhang, X. Dong, pH-triggered and enhanced simultaneous photodynamic and photothermal therapy guided by photoacoustic and photothermal imaging, Chem. Mater. 29 (2017) 5216–5224.

[34] Y. Xu, M. Zhao, L. Zou, L. Wu, M. Xie, T. Yang, S. Liu, W. Huang, Q. Zhao, Highly stable and multifunctional aza-BODIPY-based phototherapeutic agent for anticancer treatment, ACS Appl. Mater. Interfaces 10 (2018) 44324–44335.

[35] W. Xiao, P. Wang, C. Ou, X. Huang, Y. Tang, M. Wu, W. Si, J. Shao, W. Huang, X. Dong, 2-Pyridone-functionalized Aza-BODIPY photosensitizer for imaging-guided sustainable phototherapy, Biomaterials 183 (2018) 1–9.

[36] J. Zhang, H. Huang, L. Xue, L. Zhong, W. Ge, X. Song, Y. Zhao, W. Wang, X. Dong, On-demand drug release nanoplatform based on fluorinated aza-BODIPY for imaging-guided chemo-phototherapy, Biomaterials 256 (2020), 120211.

[37] A. Gorman, J. Killoran, C. O'Shea, T. Kenna, W.M. Gallagher, D.F. O'Shea, In vitro demonstration of the heavy-atom effect for photodynamic therapy, J. Am. Chem. Soc. 126 (2004) 10619–10631.

[38] D. Wu, D.F. O'Shea, Synthesis and properties of BF2-3,3'-dimethyldiarylazadipyrromethene near-infrared fluorophores, Org. Lett. 15 (2013) 3392–3395.

[39] Y. Su, Q. Hu, D. Zhang, Y. Shen, S. Li, R. Li, X.-D. Jiang, J. Du, 1,7-Di-tert-butyl-Substituted aza-BODIPYs by low-barrier rotation to enhance a photothermal-photodynamic effect, Chem. Eur J. 28 (2022), e202103571.

[40] C. Schäfer, J. Mony, T. Olsson, K. Börjesson, Effect of the aza-N-bridge and push-pull moieties: a comparative study between BODIPYs and aza-BODIPYs, J. Org. Chem. 87 (2022) 2569–2579.

[41] T. Yu, D. Zhang, J. Wang, C. Sun, T. Cui, Z. Xu, X.-D. Jiang, J. Du, Near-infrared upper phenyl-fused BODIPY as a photosensitizer for photothermal-photodynamic therapy, J. Mater. Chem. B 10 (2022) 3048–3054.

[42] Y. Wang, D. Zhang, J. Wang, D. Xi, Z. Xu, X.-D. Jiang, J. Du, Near-infrared vinyl-containing aza-BODIPY nanoparticles as photosensitizer for phototherapy, Dyes Pigments 198 (2022), 110026.

[43] C. Li, H. Ge, D. Zhang, C. Sun, S. Yue, X.-D. Jiang, J. Du, A dual channel fluorescent probe with pH-based specificity to lysosomes for multicolor imaging and localization, Sen. Actuators B 344 (2021), 130213.

[44] C. Shi, M. Li, Z. Zhang, Q. Yao, K. Shao, F. Xu, N. Xu, H. Li, J. Fan, W. Sun, J. Du, S. Long, J. Wang, X. Peng, Catalase-based liposomal for reversing immunosuppressive tumor microenvironment and enhanced cancer chemo-photodynamic therapy, Biomaterials 233 (2020), 119755.

[45] D. Xi, M. Xiao, J. Cao, L. Zhao, N. Xu, S. Long, J. Fan, K. Shao, W. Sun, X. Yan, X. Peng, NIR light-driving barrier-free group rotation in nanoparticles with an 88.3% photothermal conversion efficiency for photothermal therapy, Adv. Mater. (2020), 1907855.

[46] C. Wang, W. Chi, Q. Qiao, D. Tan, Z. Xu, X. Liu, Twisted intramolecular charge transfer (TICT) and twists beyond TICT: from mechanisms to rational designs of bright and sensitive fluorophores, Chem. Soc. Rev. 50 (2021) 12656–12678.

[47] J.R. Melamed, R.S. Edelstein, E.S. Day, Elucidating the fundamental mechanisms of cell death triggered by photothermal therapy, ACS Nano 9 (2015) 6–11.

[48] M. Perez-Hernandez, P. Del Pino, S.G. Mitchell, M. Moros, G. Stepien, B. Pelaz, W.J. Parak, E.M. Galvez, J. Pardo, J.M. de la Fuente, Dissecting the molecular mechanism of apoptosis during photothermal therapy using gold nanoprisms, ACS Nano 9 (2015) 52–61.

[49] X.-D. Jiang, X. Liu, T. Fang, C. Sun, Synthesis and application of methylthio-substituted BODIPYs/aza-BODIPYs, Dyes Pigments 146 (2017) 438–444.

[50] R. Li, T. Cui, X.-D. Jiang, Synthesis and photothermal properties of SMe-containing aza-BODIPY dye, J. Shenyang Univ. Chem. Tech. 36 (2022) 97–104.

[51] Y. Su, N. Xu, C. Wang, Q. Qiao, R. Li, D. Zhang, X. Liu, Z. Xu, X.-D. Jiang, Synthesis and application of a new BF_2-3,5-ditertbutylazadipyrromethene dye: limit autologous redox reaction of -*tBu* substituted nitroso pyrrole, J. Am. Chem. Soc. Submitted (2022).

[52] S. Li, M. Lv, J. Wang, D. Zhang, Z. Xu, X.-D. Jiang, Near-infrared absorbing aza-BODIPYs with 1,7-di-tert-butyl groups by low-barrier rotation for photothermal application, Mater. Adv. 3 (2022) 1254–1262.

[53] X. Peng, F. Song, E. Lu, Y. Wang, W. Zhou, J. Fan, Y. Gao, Heptamethine cyanine dyes with a large Stokes shift and strong fluorescence: a paradigm for excited-state intramolecular charge transfer, J. Am. Chem. Soc. 127 (2005) 4170–4171.

[54] H. Lu, J. Mack, Y. Yang, Z. Shen, Structural modification strategies for the rational design of red/NIR region BODIPYs, Chem. Soc. Rev. 43 (2014) 4778–4823.

[55] Y. Tian, H. Zhou, Q. Cheng, H. Dang, H. Qian, C. Teng, K. Xie, L. Yan, Stable twisted conformation aza-BODIPY NIR-II fluorescent nanoparticles with ultra-large Stokes shift for imaging-guided phototherapy, J. Mater. Chem. B. 10 (2022) 707–716.

[56] Q. Zou, M. Abbas, L. Zhao, S. Li, G. Shen, X. Yan, Biological photothermal nanodots based on self-assembly of peptide-porphyrin conjugates for antitumor therapy, J. Am. Chem. Soc. 139 (2017) 1921–1927.

[57] D. Wang, M.M.S. Lee, W. Xu, G. Shan, X. Zheng, R.T.K. Kwok, J.W.Y. Lam, X. Hu, B.Z. Tang, Boosting non-radiative decay to do useful work: development of a multi-modality theranostic system from an AIEgen, Angew. Chem., Int. Ed. 58 (2019) 5628–5632.

[58] Z. Yu, J. Zhou, X. Ji, G. Lin, S. Xu, X. Dong, W. Zhao, Discovery of a monoiodo aza-BODIPY near-infrared photosensitizer: in vitro and in vivo evaluation for photodynamic therapy, J. Med. Chem. 63 (2020) 9950–9964.

[59] T. Hosokai, H. Matsuzaki, H. Nakanotani, K. Tokumaru, T. Tsutsui, A. Furube, K. Nasu, H. Nomura M. Yahiro, C. Adachi, Evidence and mechanism of efficient thermally activated delayed fluo-rescence promoted by delocalized excited states, Sci. Adv. 3 (2017), e1603282.

[60] T. Montagnon, M. Tofu, G. Vassilikogiannakis, Using singlet oxygen to synthesize polyoxygenated natural products from furans, Acc. Chem. Res. 41 (2008) 1001–1011.

[61] H. Ma, S. Long, J. Cao, F. Xu, P. Zhou, G. Zeng, X. Zhou, C. Shi, W. Sun, J. Du, K. Han, J. Fan, X. Peng, New Cy5 photosensitizers for cancer phototherapy: a low singlet-triplet gap provides high quantum yield of singlet oxygen, Chem. Sci. 12 (2021) 13809–13816.

[62] X. Cai, B. Liu, Aggregation-induced emission: recent advances in materials and biomedical applications, Angew. Chem. Int. Ed. 59 (2020) 9868–9886.

[63] X. Fu, Y. Huang, H. Zhao, E. Zhang, Q. Shen, Y. Di, F. Lv, L. Liu, S. Wang, Near-infrared-light remote-controlled activation of cancer immunotherapy using photothermal conjugated polymer nanoparticles, Adv. Mater. 33 (2021), e2102570.

[64] W. Ma, Q. Chen, W. Xu, M. Yu, Y. Yang, B. Zou, Y.S. Zhang, J. Ding, Z. Yu, Self-targeting visualizable hyaluronate nanogel for synchronized intracellular release of doxorubicin and cisplatin in combating multidrug-resistant breast cancer, Nano Res. 14 (2021) 846–857.

[65] M. He, L. Yu, Y. Yang, B. Zou, W. Ma, M. Yu, J. Lu, G. Xiong, Z. Yu, A. Li, Delivery of triptolide with reduction-sensitive polymer nanoparticles for liver cancer therapy on patient-derived xenografts models, Chin. Chem. Lett. 31 (2020) 3178–3182.

[66] J. Huang, Y. Huang, Z. Xue, S. Zeng, Tumor microenvironment responsive hollow mesoporous Co_9S_8@MnO_2-ICG/DOX intelligent nanoplatform for synergistically enhanced tumor multimodal therapy, Biomaterials 262 (2020), 120346.

[67] Y. Xu, S. Wang, Z. Chen, R. Hu, S. Li, Y. Zhao, L. Liu, J. Qu, Highly stable organic photothermal agent based on near-infrared-II fluorophores for tumor treatment, J. Nanobiotechnol. 19 (2021) 37.

[68] Y. Cai, Z. Wei, C. Song, C. Tang, W. Han, X. Dong, Optical nano-agents in the second near-infrared window for biomedical applications, Chem. Soc. Rev. 48 (2019) 22–37.